

# Parameterization of the energy and rapidity distributions of secondary pions and kaons produced in energetic proton – proton collisions

Hylke B. J. Koers,<sup>1,2,\*</sup> Asaf Pe'er,<sup>3</sup> and Ralph A. M. J. Wijers<sup>3</sup>

<sup>1</sup>*NIKHEF, P.O. Box 41882, 1009 DB Amsterdam, The Netherlands*

<sup>2</sup>*University of Amsterdam, Amsterdam, The Netherlands*

<sup>3</sup>*Astronomical Institute ‘Anton Pannekoek’, Faculty of Science,  
University of Amsterdam, Kruislaan 403, 1098 SJ Amsterdam, The Netherlands*

(Dated: September 7, 2018)

The possibility of proton acceleration to very high energies in astrophysical sources may have unique observational consequences. In particular, the decay of secondary mesons created in the interaction of energetic protons with photons or nucleons gives rise to high-energy gamma rays and neutrinos with potentially observable fluxes. Recently, there has been considerable interest in the parameterization of the energy spectra of these secondaries. Less attention has been paid to the angular distributions, which may have an important effect on observational quantities and are required to address collisions between protons with different energies and an arbitrary scattering angle. In this work, we study the complete particle distributions of secondary mesons created in proton – proton collisions. We present parameterizations of the energy and rapidity distributions of secondary pions and kaons that reproduce results generated with the event generator PYTHIA to within  $\sim 10\%$  in the bulk of the parameter space. The parameterizations are based on incident proton energies from 1 TeV to 1 PeV and are suited for extrapolation to higher energies. We present several applications of these parameterizations. Energy spectra and angular distributions of stable decay products (electrons, neutrinos and gamma rays) follow readily. We give an example of the gamma-ray spectrum that results from the decay of  $\pi^0$  mesons created in a proton – proton collision. We show that there is a strong correlation between the energy of secondary mesons and the degree of collimation around the direction of the colliding protons. This effect may have important implications for the detection possibility of neutrinos created in the interaction of a developing GRB with its surroundings.

PACS numbers: 13.60.Le, 25.40.Ep, 13.85.-t, 98.70.Sa

## I. INTRODUCTION

The possibility of proton acceleration to very high energies in astrophysical sources may provide unique observational opportunities. The interaction of energetic protons with photons or nucleons results in copious production of secondary mesons decaying into high-energy gamma rays and neutrinos that can be observed with current and future detectors. The recently observed TeV gamma-ray emission from supernova remnant RX J1713.7-3946 [1] has been attributed to this mechanism [2], although such an origin is still under debate [3]. TeV gamma rays have been reported in coincidence with gamma-ray burst (GRB) 970417a [4, 5] but also in this case it is not established whether the origin is hadronic [6].

The existence of astrophysical proton accelerators is indicated by observations of high-energy cosmic rays (CRs). There is evidence for a substantial proton component above the ‘knee’ at  $\sim 4 \times 10^6$  GeV in the cosmic-ray spectrum (see e.g. Ref. [7] for a review). Observations of extensive air showers due to CRs with energies up to  $\sim 10^{11}$  GeV are consistent with nucleon primaries, al-

though other primaries are also possible (e.g., Ref. [8]).

Various astrophysical systems have been suggested as CR sources. Galactic supernova remnants are the leading candidate for the generation of CRs with energies up to  $\sim 10^8$  GeV (see e.g. Ref. [9]). Several extragalactic sources have been considered as possible sources of higher energy CRs, such as active galactic nuclei [10] (see however Ref. [11]), hot spots of Fanaroff-Riley class II radio galaxies [11, 12], pulsars [13] and GRBs [14, 15].

A population of high-energy protons in these sources would carry a rich phenomenology. In GRBs for example, the interaction of accelerated protons with GRB photons leads to  $\sim 10^5$  GeV neutrinos [16] and to  $\sim 10^2 - 10^3$  GeV gamma rays [6, 17]. High-energy proton interactions may play an important role in the interaction of a developing GRB with its environment, e.g. when the fireball has not yet emerged from the stellar surface [18, 19] or when energetic GRB protons collide with cold protons in the GRB surroundings [20, 21, 22].

Detailed parameterizations of the energy spectra of secondary particles created in proton – proton ( $pp$ ) collisions are essential in the study of particle production in astrophysical proton accelerators. Such parameterizations were recently presented by Kamae et al. [23] and Kelner, Aharonian and Bugayov [24]. However, the parameterizations presented by these authors do not include the angular distributions of the secondary particles. As a consequence, these parameterizations can only

---

\*Electronic address: hkoers@nikhef.nl

be applied to the scattering geometry for which they were derived, viz. with a target proton at rest. This is sufficient if one of the protons is at rest in the observer frame, but a more general treatment is required if the bulk of the protons can be accelerated.

The parameterization of the complete particle distributions is an important generalization because this provides, through Lorentz transformations, secondary particle distributions and energy spectra after a collision of two protons with arbitrary energies and an arbitrary incident angle. Such a parameterization can therefore be applied to any acceleration scenario. A second advantage is that the full distribution includes correlations between the energy and the angle of outgoing particles, which may have important effects on observable quantities in a non-isotropic environment.

Badhwar, Stephens and Golden [25], Stephens and Badhwar [26] and Blattnig et al. [27] have presented parameterizations of the complete distributions of charged and neutral pions and charged kaons created in  $pp$  collisions. However, these parameterizations are valid for incident proton energies  $E_p \lesssim 2 \times 10^3$  GeV, which is much lower than the highest proton energies  $\sim 10^{11}$  GeV expected in accelerating astrophysical sources.

In this paper we study the complete distributions of secondary particles produced in  $pp$  collisions through Monte Carlo simulations. We consider a proton with energy  $10^3$  GeV  $< E_p < 10^6$  GeV that collides with a proton at rest, which corresponds to center-of-mass energy  $43$  GeV  $< \sqrt{s} < 1.4 \times 10^3$  GeV. We assume that the distribution of a secondary particle species is invariant under rotations around the collision axis, which implies that the distribution is fully parameterized with two independent kinematical variables. We present parameterizations of the energy and rapidity distributions of secondary pions and kaons. The parameterizations are based on Monte Carlo data in the simulated energy range but can be applied to collisions of protons with higher energies.

We consider only secondary pions and kaons and not their stable decay products, viz. electrons, neutrinos and gamma rays. This approach separates the physics in the  $pp$  collision from subsequent decay processes. Energy spectra and particle distributions of the resulting stable daughter particles are readily found from our results (either analytically or as part of a computer code) and the well-known decay spectra of pions and kaons (see e.g. Refs. [24, 28]). We do not separately consider short-lived mesons (such as  $\eta$ ,  $\rho$  or  $\omega$ ) because their lifetime is much shorter than that of charged kaons and pions. The decay products of these mesons, mostly pions and gamma rays, are grouped together with the prompt secondaries. The restriction to the  $pp$  interaction *per se* gives our results a broad applicability. For example, it has been pointed out recently [29, 30] that energy losses of pions and kaons can leave an imprint on the energy spectra of the daughter particles in GRB jets. A proper treatment of this effect requires knowledge of the pion and kaon distributions.

Hadron interactions have a complex phenomenology

due to the compositeness of the ingoing and outgoing particles. It is currently not possible to compute the cross section or the resulting particle distribution from first principles. Therefore, detailed studies of particle production in hadron interactions require the use of event generators. In this work, we simulate the  $pp$  interaction with the event generator PYTHIA [31], which is tested against experimental data. It is capable of simulating various incident and target particles so that it is possible to extend this work to proton – neutron and proton – photon interactions with essentially the same code. PYTHIA uses the ‘Lund string model’ [32] to describe the process of secondary meson formation.

This paper is organized as follows: in section II, we present experimental data on the  $pp$  cross section and the charged multiplicity, i.e. the number of charged particles created in a single inelastic collision. In section III we discuss the kinematics of the simulated interaction and introduce the particle distribution with respect to energy and rapidity. Details on the event simulation with PYTHIA and the fitting procedure are discussed in section IV. In section V, we present a comparison between PYTHIA results and experimental data and we present the parameterizations of the energy spectra and particle distributions of secondary pions and kaons. Applications of these parameterizations are considered in section VI. We demonstrate through explicit examples how the parameterizations can be used to study particle production in collisions of protons with different energies and an arbitrary incident angle. We also present an example in which we derive the gamma-ray energy spectrum resulting from  $\pi^0 \rightarrow \gamma\gamma$  decay. In section VII, we discuss the application of the parameterizations to incident protons with very high energies. We discuss the results in section VIII. Conclusions are presented in section IX.

## II. EXPERIMENTAL DATA ON THE CROSS SECTION AND SECONDARY MULTIPLICITY IN PROTON – PROTON INTERACTIONS

In this section, we discuss experimental data on the cross section of  $pp$  interactions and on the number of charged particles created in a  $pp$  interaction. The data presented in this section are used in section V to validate our numerical method.

### A. Cross section

Proton – proton interactions are usually separated into elastic scattering, in which no particles are created; diffractive interactions, in which the energy transfer between the protons is small; and inelastic non-diffractive interactions, in which the energy transfer is large enough for the constituent quarks and gluons to interact. The total  $pp$  cross section  $\sigma_{\text{tot}}$  can be expanded in terms of

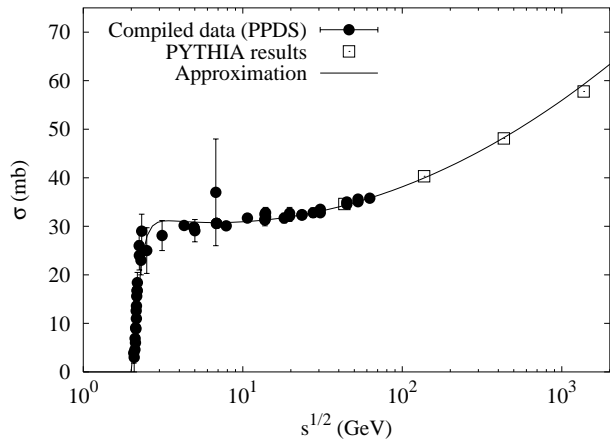


FIG. 1: Comparison between the inelastic  $pp$  cross section calculated with PYTHIA (open squares) and experimental data (disks). The solid line represents the fit given in eq. (3). Experimental data is taken from the PPDS (see footnote 1).

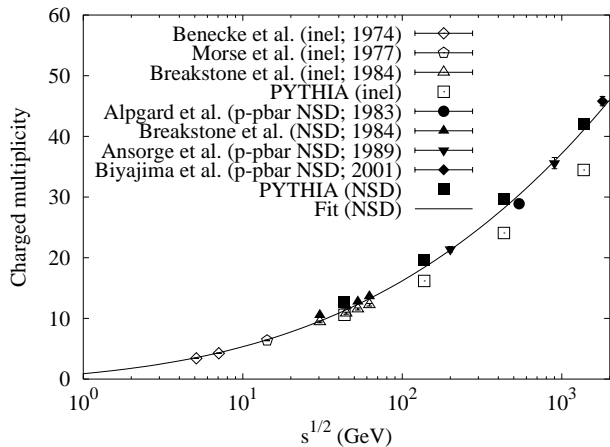


FIG. 2: Comparison between the charged multiplicity calculated with PYTHIA (squares) and experimental data (other symbols). Open symbols correspond to inelastic processes (inel), solid symbols correspond to non-single-diffractive (NSD) processes. The solid line shows the approximation given in eq. (5).

these processes as

$$\sigma_{\text{tot}} = \sigma_{\text{nd}} + \sigma_{\text{sd}} + \sigma_{\text{dd}} + \sigma_{\text{el}}, \quad (1)$$

where  $\sigma_{\text{nd}}$ ,  $\sigma_{\text{sd}}$ ,  $\sigma_{\text{dd}}$  and  $\sigma_{\text{el}}$  are the cross section for non-diffractive processes (the hard QCD processes), single diffraction ( $AB \rightarrow XB$  or  $AB \rightarrow AX$ ), double diffraction ( $AB \rightarrow XY$ ), and elastic scattering ( $AB \rightarrow AB$ ) respectively. In this work we do not explicitly separate diffractive and non-diffractive processes because we are mostly interested in astrophysical applications where it will be impossible to distinguish between these components; see Ref. [23] for a separate treatment.

We are primarily interested in the inelastic  $pp$  cross

section  $\sigma_{\text{inel}} = \sigma_{\text{nd}} + \sigma_{\text{sd}} + \sigma_{\text{dd}}$  because all processes that create secondary particles are contained in this quantity. At energies above the threshold energy  $E_{\text{th}} = 1.22$  GeV and below  $\sqrt{s} = 3 \times 10^4$  GeV, the inelastic cross section for a proton with energy  $E_p$  interacting with a target proton at rest can be fitted with [24]:

$$\sigma_{\text{inel}}^{\text{fit}}(E_p) = \left( 33.24 - 3.624 \log E_p + 1.325 (\log E_p)^2 \right) \times \left( 1 - \left( \frac{E_{\text{th}}}{E_p} \right)^4 \right)^2 \text{ mb}, \quad (2)$$

where  $E_p$  is measured in GeV. In deriving this formula, it is assumed that the ratio of the inelastic cross section to the total cross section, which for energies  $43 \text{ GeV} < \sqrt{s} < 63 \text{ GeV}$  is given by [33]

$$\sigma_{\text{tot}} = 1.21 \sigma_{\text{inel}}, \quad (3)$$

holds for higher energies  $63 \text{ GeV} < \sqrt{s} < 3 \times 10^4 \text{ GeV}$  as well. The incident proton energy  $E_p$  in eq. (2) is related to the center-of-mass energy  $\sqrt{s}$  as

$$E_p = \frac{s}{2m_p c^2} - m_p c^2, \quad (4)$$

where  $m_p$  is the proton mass. In figure 1, we show the approximation given in eq. (2) together with PYTHIA results (see section V below) and the available experimental data.<sup>1</sup> This shows the validity of approximation (2).

## B. Secondary multiplicity

Bubble chamber and accelerator experiments have shown that the number of charged particles created in proton – (anti)proton collisions, i.e. the charged multiplicity, increases as a function of the incident proton energy.<sup>2</sup> We find that up to the highest energies currently accessible,  $\sqrt{s} \leq 1.8 \times 10^3$  GeV, the charged particle multiplicity in non-diffractive  $pp$  interactions is well fitted with

$$\mathcal{M}_{\text{ch}}^{\text{fit}}(s) = 0.89 + 1.24 \log s + 0.34 \log^2 s + 0.077 \log^3 s. \quad (5)$$

This functional form is an extension of an approximation due to Matthiae [36] (see also Ref. [35]) which is valid only up to  $\sqrt{s} \leq 540$  GeV. The last logarithmic term, which does not appear in the approximation by Matthiae,

<sup>1</sup> A compilation of experimental data on the inelastic  $pp$  cross section is available at the Particle Physics Data System (PPDS) website <http://wwwppds.ihep.su:8001/>. In producing figure 1, we have not considered experimental data that is marked with the warning comment ‘W’.

<sup>2</sup> The charged particle multiplicity in  $pp$  and  $p\bar{p}$  interactions is virtually identical at ISR energies  $\sqrt{s} = 53$  GeV (Ref. [34]; see also Ref. [35]).

is required in order to fit the multiplicity at both high and low energies. We present in figure 2 experimental data<sup>3</sup> together with the approximation given in eq. (5) and PYTHIA results (see section V below).

A logarithmic dependence  $\mathcal{M}_{\text{ch}} \propto \log s$  is commonly interpreted as due to an increase in phase space because the range of allowed rapidities scales as  $\log(s/m^2c^4)$  (e.g., Ref. [35]). A stronger increase in secondary multiplicity is then attributed to an additional rise in the level of the observed central rapidity plateau, the origin of which is not understood from first principles.

At high energies, data on the neutral particle multiplicity is sparse because of experimental difficulties. As a result, there is no fit to the neutral particle multiplicity that extends to  $\sqrt{s} \gtrsim 50$  GeV which is based on experimental data. A fit to the separate multiplicities of both charged and neutral pions and charged kaons created in  $pp$  collisions for center-of-mass energies  $\sqrt{s} < 53$  GeV was presented in Ref. [44].

The scarcity of experimental data on separate particle multiplicities at high energies motivates the use of event generators such as PYTHIA. In section V A, we show that PYTHIA correctly reproduces experimental results on the total charged multiplicity. In section V B, we present a fit to PYTHIA results on charged and neutral pion and kaon multiplicities in the energy range  $43 \text{ GeV} < \sqrt{s} < 1.4 \times 10^3 \text{ GeV}$ .

### III. KINEMATICS AND SECONDARY PARTICLE DISTRIBUTION

In this and the following sections, we consider an energetic proton that moves along the  $z$ -axis and collides with a proton at rest, i.e. a fixed target. This scattering geometry is referred to as the lab frame. We use  $p_z$  to denote a longitudinal momentum, along the  $z$ -axis, and  $p_T$  to denote a transverse momentum.

#### A. Kinematics

Assuming that the secondary particle distribution is symmetric around the collision axis, the phase space of the outgoing particles is fully parameterized with two independent kinematical variables. Here, we choose the energy  $\epsilon$  and the rapidity  $y$ , which is defined as

$$y = \frac{1}{2} \ln \left( \frac{\epsilon + p_z c}{\epsilon - p_z c} \right) \Leftrightarrow \tanh y = \frac{p_z c}{\epsilon}. \quad (6)$$

For given particle energy  $\epsilon$ , the rapidity cannot take any value. The mass-shell relation implies that  $-y_1 < y < y_1$ , where

$$y_1 = \text{arccosh} \left( \frac{\epsilon}{m c^2} \right), \quad (7)$$

and  $m$  is the secondary (pion or kaon) mass. A second requirement follows from energy conservation in the  $pp$  collision. If the energy of the secondary particle  $\epsilon > m_p c^2$ , the rapidity is additionally bounded by  $y > y_2$ , where

$$y_2 = \text{arctanh} \left( \frac{1}{\beta'_p} - \frac{2m_p c^2}{\beta'_p \epsilon} \right). \quad (8)$$

In this equation  $\beta'_p$  is the proton velocity in the center-of-mass frame in units of  $c$ , which we take to be equal to one for incident proton energies  $E_p \gg m_p c^2$  in the following calculations. Note that eq. (7) can be applied in any frame, while eq. (8) only holds in the lab frame.

#### B. Secondary particle distribution

We are interested in the particle distribution for one-pion and one-kaon inclusive processes,

$$pp \rightarrow XY, \quad (9)$$

where  $X$  denotes a single pion or a single kaon and  $Y$  may be any combination of particles with the appropriate quantum numbers. We denote by  $n(\epsilon, y) d\epsilon dy$  the number of created particles of a given species with energy and rapidity in the range  $(\epsilon \dots \epsilon + d\epsilon) \times (y \dots y + dy)$ :

$$n(\epsilon, y) = \frac{d^2 N}{d\epsilon dy} = \frac{1}{\sigma_{\text{inel}}} \frac{d^2 \sigma}{d\epsilon dy}, \quad (10)$$

where  $\sigma_{\text{inel}} = \sigma_{\text{nd}} + \sigma_{\text{sd}} + \sigma_{\text{dd}}$  is the inelastic  $pp$  cross section and  $\sigma$  is the inclusive cross section to detect a particle of a given kind (assuming an ideal detector). This cross section is equal to the weighted sum of  $n$ -particle exclusive cross sections  $\sigma_n$  (i.e., the cross section to create exactly  $n$  particles)<sup>4</sup>:

$$\sigma = \sum_n n \sigma_n = \mathcal{M} \sigma_{\text{inel}}, \quad (11)$$

where  $\mathcal{M} = \mathcal{M}(s)$  is the multiplicity of the given particle species. The particle distribution  $n(\epsilon, y)$  is related to the Lorentz invariant differential cross section  $\epsilon d^3 \sigma / dp^3$ ,

<sup>3</sup> The experimental data is taken from Refs. [37, 38, 39, 40, 41, 42]. The data at  $\sqrt{s} = 1.8 \times 10^3$  GeV is obtained by the E735 experiment [43], which does not cover the full particle phase space. We use results from Ref. [40], who have determined the charged particle multiplicity through a fit to experimental data on the multiplicity distribution.

<sup>4</sup> We do not consider the exclusive cross sections separately because we are interested in particle creation by all processes together. To a first approximation, the relative sizes of the  $n$ -particle exclusive cross sections depend on energy only through the total multiplicity [45]. This ‘KNO scaling’ is known to be violated at energies  $\gtrsim 500$  GeV [38, 46].

which is often used to represent experimental data, as follows:

$$n(\epsilon, y) = \frac{2\pi}{c} \left( \frac{m^2 + p_T^2}{\sigma_{\text{inel}}\epsilon} \right) \left( \epsilon \frac{d^3\sigma}{d^2p_T dp_z} \right). \quad (12)$$

#### IV. NUMERICAL METHOD

##### A. Configuration of the PYTHIA event generator and initial conditions

The  $pp$  interaction is simulated with PYTHIA version 6.324 using default values for most of the control parameters. Elastic and diffractive processes are included by selecting MSEL=2. In comparing PYTHIA results to experimental data on the cross section and charged multiplicity, we allow for pion and kaon decay. In determining the parameterizations of the particle distributions, pion and kaon decay are switched off with the command MDCY(PYCOMP(ID),1)=0, where ID is the corresponding particle identification number. This approach separates the physics in the  $pp$  collision from subsequent processes, such as secondary synchrotron emission prior to decay, etc.

The PYTHIA code relies on the Lund string model [32] to determine the distribution and multiplicity of secondary particles. We present a brief discussion of this model in appendix A; more details can be found in the PYTHIA manual [31].

We simulate  $pp$  collisions for incident proton energies  $E_p = 10^3$  GeV,  $E_p = 10^4$  GeV,  $E_p = 10^5$  GeV and  $E_p = 10^6$  GeV colliding with a proton at rest. For higher values of the incident proton energy, PYTHIA signals a loss of accuracy in kinematical variables in some of the generated events.

##### B. Fitting procedure

The secondary particle distributions are discretized, spanning the full range of available energy and kinematically allowed rapidity. In this process, the energy is divided into 200 bins with size  $\Delta\epsilon_i$  with a logarithmic division and the rapidity is divided into 100 bins with size  $\Delta y_i$  with a linear division. The logarithmic energy division is chosen because we consider up to seven energy decades; the rapidity division is linear because the range of allowed rapidities scales with the logarithm of energy. The number of bins is limited by computational issues, as data files become increasingly large and fitting becomes increasingly time-consuming with an increasing number of bins. We have verified that this number of bins is sufficient for convergence of the resulting parameterization.

We use MINUIT<sup>5</sup> as a minimization algorithm for the

weighted squared difference between the PYTHIA results and the particle distribution fit function  $n(\epsilon, y)$ .<sup>6</sup> We consider only statistical errors in the PYTHIA results. We simulate  $N_{\text{ev}} = 10^6$  collisions for every incident proton energy, which results in a statistical error of a few percent near the maximum values of  $\epsilon n(\epsilon, y)$ . We compare our results with parameterizations based on other event generators to obtain an estimate of the importance of systematic uncertainties within the models underlying PYTHIA in section VIII A.

The relative deviation between a PYTHIA data point  $n_i$  and the fitted value  $n(\epsilon_i, y_i)$  is expressed as

$$\delta_i = \frac{n(\epsilon_i, y_i) - n_i}{n_i}, \quad (13)$$

where  $n_i$  is the number of particles in a bin with average energy  $\epsilon_i$  and average rapidity  $y_i$  divided by the bin size  $\Delta\epsilon_i \times \Delta y_i$ . We note that the deviations are expected to follow a Gaussian distribution with average value

$$\langle \delta_i \rangle \propto \sqrt{\frac{1}{\epsilon_i n_i}}, \quad (14)$$

where the dependence on energy is due to the logarithmic energy binning. In particular, the average deviation size is expected to be roughly independent of energy for a  $n(\epsilon) \propto \epsilon^{-1}$  energy spectrum.

#### V. RESULTS

##### A. Comparison of PYTHIA results with experimental data

We show in figures 1 and 2 experimental data on the  $pp$  cross section and charged multiplicity together with PYTHIA results. In producing these figures, we have not switched off any natural particle decays in the PYTHIA simulations in order to compare PYTHIA results with experimental data (cf. section IV A).

We observe from figure 1 that the PYTHIA cross sections are compatible with an extrapolation of the experimental data (see footnote 1) in the energy range  $43 \text{ GeV} < \sqrt{s} < 1.4 \times 10^3 \text{ GeV}$ . In figure 2, we show a comparison between experimental data and PYTHIA results on the charged multiplicity. In this work, we are interested in particle creation by all inelastic processes. However, experimental data on the charged multiplicity resulting from all inelastic processes is available only up to  $\sqrt{s} = 62 \text{ GeV}$  [39, 41, 42]. Experimental data on the charged multiplicity resulting from the restricted

---

umentation is available on the website <http://wwwasdoc.web.cern.ch/wwwasdoc/minuit/>

<sup>6</sup> We do not explicitly write the dependence of  $n$  on  $E_p$  here and in the following sections.

---

<sup>5</sup> CERN Program Library entry D506; doc-

TABLE I: Average fraction of the incident proton energy carried by the outgoing particle species.

$N_p$	$N_s$	$\gamma$	$\pi^+$	$\pi^-$	$\pi^0$	$K^+$	$K^-$	$K^0$	$\overline{K^0}$	
$f$	0.56	0.033	0.013	0.13	0.095	0.12	0.016	0.011	0.014	0.011

TABLE II: Numerical values for the constants in the multiplicity approximation formula (15).

	$\pi^+$	$\pi^-$	$\pi^0$	$K^+$	$K^-$	$K^0$	$\overline{K^0}$
$c_0$	4.5	3.8	4.9	0.49	0.32	0.36	0.29
$c_1$	-1.7	-1.7	-2.1	-0.23	-0.20	-0.17	-0.18
$c_2$	0.50	0.50	0.58	0.063	0.060	0.054	0.054

class of non-single-diffractive (NSD) interactions is available up to much higher energies  $\sqrt{s} = 1.8 \times 10^3$  GeV [37, 40, 41, 47]. To verify our numerical method, we have performed a separate simulation<sup>7</sup> of NSD interactions to compare the NSD charged multiplicity with experimental data. We show in figure 2 that the PYTHIA results on the charged multiplicity due to both inelastic processes and NSD processes are compatible with experimental data.

### B. Average secondary energy and multiplicity

The fraction  $f$  of the incident proton energy carried by a certain secondary particle species is virtually independent of the incident proton energy (see Ref. [48]). The average fractions for nucleons, photons, pions and kaons found by PYTHIA simulations are given in table I. In this table,  $N_p$  and  $N_s$  denote primary and secondary nucleons, respectively (see below). Other possible secondaries (direct electrons, muons, neutrinos) together carry less than 0.1% of the incident proton energy.

We define the primary nucleon as the most energetic outgoing nucleon. The probability that the primary nucleon is a proton is 0.70; if it is a proton, it carries an average fraction 0.63 of the incident proton energy. The probability that the primary nucleon is a neutron is 0.30; if this is the case, the average energy fraction is 0.41. The energy fraction carried by the primary nucleon as shown in table I represents the weighted average.

We fit PYTHIA results on the secondary particle multiplicities within the energy range  $43 \text{ GeV} < \sqrt{s} < 1.4 \times 10^3 \text{ GeV}$ . We find that both charged and neutral pion and kaon multiplicities are well approximated with the following function:

$$\mathcal{M}_i = c_0 + c_1 \log s + c_2 \log^2 s, \quad (15)$$

<sup>7</sup> For the NSD case, we have switched off single diffraction in the event generation with the commands `MSUB(92)=0` and `MSUB(93)=0`.

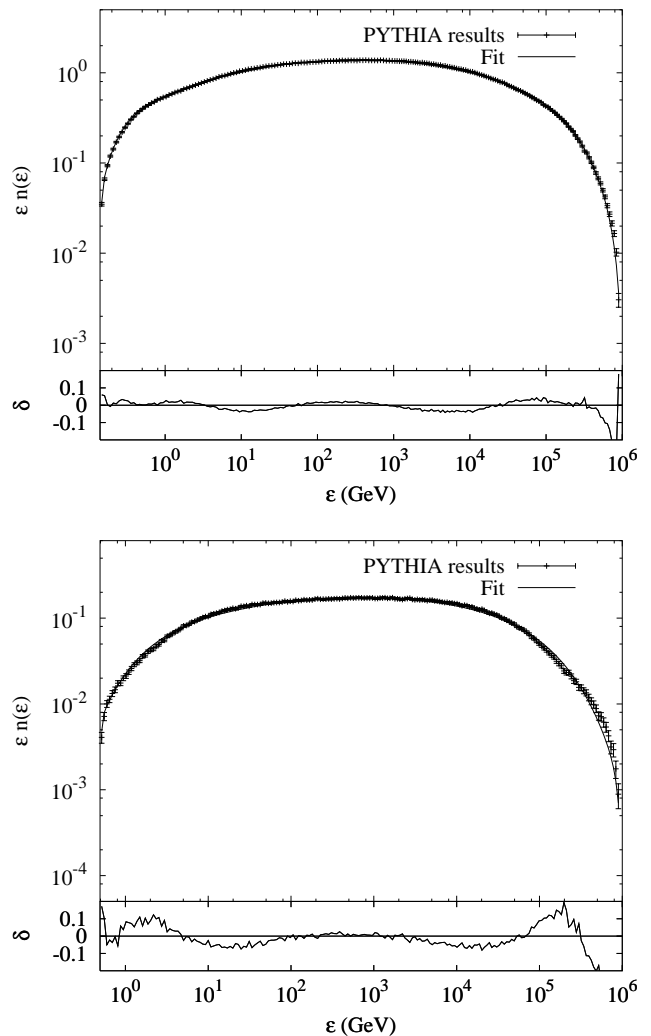


FIG. 3: Energy spectra of  $\pi^+$  (top panel) and  $K^+$  (bottom panel) mesons created in a collision with incident proton energy  $E_p = 10^6$  GeV. Note the different scales on the vertical axes. Upper graphs: comparison of PYTHIA results and fit to the energy spectrum normalized as  $\epsilon n(\epsilon)$ ; lower graphs: deviation  $\delta_i = n(\epsilon_i, y_i)/n_i - 1$  between PYTHIA results points and fitted values.

where  $c_0$ ,  $c_1$  and  $c_2$  are numerical constants whose values are given in table II and  $s$  is expressed in units of  $\text{GeV}^2$ . The charged kaon multiplicity deduced from eq. (15) is within  $\sim 5\%$  of experimental data at  $\sqrt{s} = 45 \text{ GeV}$  [44]. The charged pion multiplicities determined by this equation are  $\sim 10\%$  lower than the experimental values. This discrepancy can be attributed to the fact that we have considered only prompt pions (i.e., excluding pions from kaon decay).

### C. Pion and kaon energy spectra

We present in figure 3 the  $\pi^+$  and  $K^+$  energy spectra resulting from a collision of a proton with incident energy  $E_p = 10^6$  GeV with a proton at rest. We find that the energy spectra for all secondary particles and incident proton energies  $10^3$  GeV  $< E_p < 10^6$  GeV are similar in shape.<sup>8</sup> To a first approximation, the energy spectra follow a  $\epsilon^{-1}$  power-law, reflecting the absence of an energy scale between the secondary mass and the maximum available energy. This is supplemented with additional functions that we denote with  $\alpha(\epsilon)$ ,  $\beta(\epsilon)$ ,  $\gamma_1(\epsilon)$  and  $\gamma_2(\epsilon)$  (here and in the following we do not explicitly write the dependence of the model parameters on the incident proton energy  $E_p$  to avoid cluttering of the notation). Thus we write the pion and kaon energy spectrum in the following way:

$$n(\epsilon) = n_0 \epsilon^{-1} \alpha(\epsilon) \beta(\epsilon) \gamma_1(\epsilon) \gamma_2(\epsilon), \quad (16)$$

where  $n_0$  is a normalization constant,  $\alpha(\epsilon)$  accounts for the convex shape on a log-log scale,  $\beta(\epsilon)$  incorporates an exponential decline at higher and lower energies,  $\gamma_1(\epsilon)$  is a strong cutoff near the mass threshold and  $\gamma_2(\epsilon)$  is a strong cutoff near the maximum available energy. These functions are parameterized as follows:

$$n_0 = 1.21 \times 10^{p_0 + p_1 p_2^2}; \quad (17a)$$

$$\alpha(\epsilon) = \epsilon^{p_1 (\log(\epsilon) - 2p_2)}; \quad (17b)$$

$$\beta(\epsilon) = 10^{-(\epsilon/\epsilon_3)^{p_3}} 10^{-(\epsilon/\epsilon_5)^{p_5}}; \quad (17c)$$

$$\gamma_1(\epsilon) = \tanh(p_{70} \log(\epsilon/mc^2)); \quad (17d)$$

$$\gamma_2(\epsilon) = \tanh(p_{80} \log(E_p/\epsilon)), \quad (17e)$$

where  $\epsilon_3 \equiv 10^{p_2 + p_4}$ ,  $\epsilon_5 \equiv 10^{p_2 + p_6}$  and all energies are expressed in units of GeV. The following parameters vary with incident proton energy:

$$p_0 = p_{00} + p_{01} \log(E_p); \quad (18a)$$

$$p_1 = p_{10} + p_{11} \log(E_p); \quad (18b)$$

$$p_2 = p_{20} + p_{21} \log(E_p); \quad (18c)$$

$$p_4 = p_{40} - p_2; \quad (18d)$$

$$p_6 = p_{60} + p_2. \quad (18e)$$

Thus, the energy spectrum of secondary pions and kaons is fully described in terms of 12 free parameters  $p_{ij}$  for every particle species. These parameters and their numerical values, which are determined by a least-squares fit, are given in table III.

For pions, deviations between fit values  $n(\epsilon_i)$  and PYTHIA results  $n_i$  are less than 5% except for very high energies ( $\epsilon \geq E_p/2$ ) and some occasional points near the mass threshold where the deviation is  $\sim 10\%$ . For

kaons, statistical fluctuations are larger since the number of kaons to pions is roughly 1:10. At intermediate energies the fit is nevertheless within  $\sim 5\%$  of PYTHIA results except for some isolated points. Near the mass threshold deviations increase to  $\sim 20\%$ ; at very high energies, where  $\epsilon n(\epsilon, y)$  is typically more than an order of magnitude smaller than its maximum value, deviations can increase to  $\sim 40\%$ . We have verified that the parameterized spectra integrate to the right multiplicities as given in eq. (15) within a few percent, except for the  $K^0$  spectrum for which the deviation is  $\sim 10\%$  at the low end of the simulated proton energy range.

### D. Pion and kaon energy and rapidity distributions

We present the pion and kaon rapidity distributions, i.e.  $n(\epsilon, y)$  at fixed  $\epsilon = \epsilon_0$ , for incident proton energy  $E_p = 10^6$  GeV and secondary particle energy  $\epsilon = 10^3$  GeV in figure 4. We find that rapidity distributions for different proton energies and different secondary particle energies are very similar in shape. This shape is different for pions and for kaons, hence we treat pions and kaons separately in the following.

#### 1. Pions

The pion rapidity distributions at fixed energy are found to be approximately Gaussian near their maximum values (see fig. 4). At intermediate pion energies,  $\epsilon \sim \sqrt{E_p}$ , the distributions exhibit a low-rapidity tail that falls off exponentially (all energies are expressed in units of GeV). The distributions fall off very steeply at the boundaries of the kinematical domain given in eqs. (7) and (8).

We factorize the full particle distribution  $n(\epsilon, y)$  into a modified energy spectrum  $\tilde{n}(\epsilon)$  and a rapidity-dependent function  $\phi(\epsilon, y)$  that contains both a Gaussian and an exponential part:

$$n_\pi(\epsilon, y) = \tilde{n}(\epsilon) \phi(\epsilon, y), \quad (19)$$

where

$$\tilde{n}(\epsilon) = n_0 \epsilon^{-1} \alpha(\epsilon) \beta(\epsilon) \gamma_2(\epsilon) 10^{q_0 + 2q_3}; \quad (20a)$$

$$\phi(\epsilon, y) = 10^{-2\sqrt{q_3 q_1^2 (y - q_2)^2 + q_3^2}}, \quad (20b)$$

and  $n_0$ ,  $\alpha(\epsilon)$ ,  $\beta(\epsilon)$  and  $\gamma_2(\epsilon)$  are defined in eqs. (17). The parameters  $q_i$  depend on the pion energy  $\epsilon$  and on the incident proton energy  $E_p$  in the following way (here and in the following we do not explicitly write the dependence of the parameters  $q_i$  on the pion and proton energies to

<sup>8</sup> Figures of these and others fits are available at <http://www.nikhef.nl/~hkoers/ppfit>.

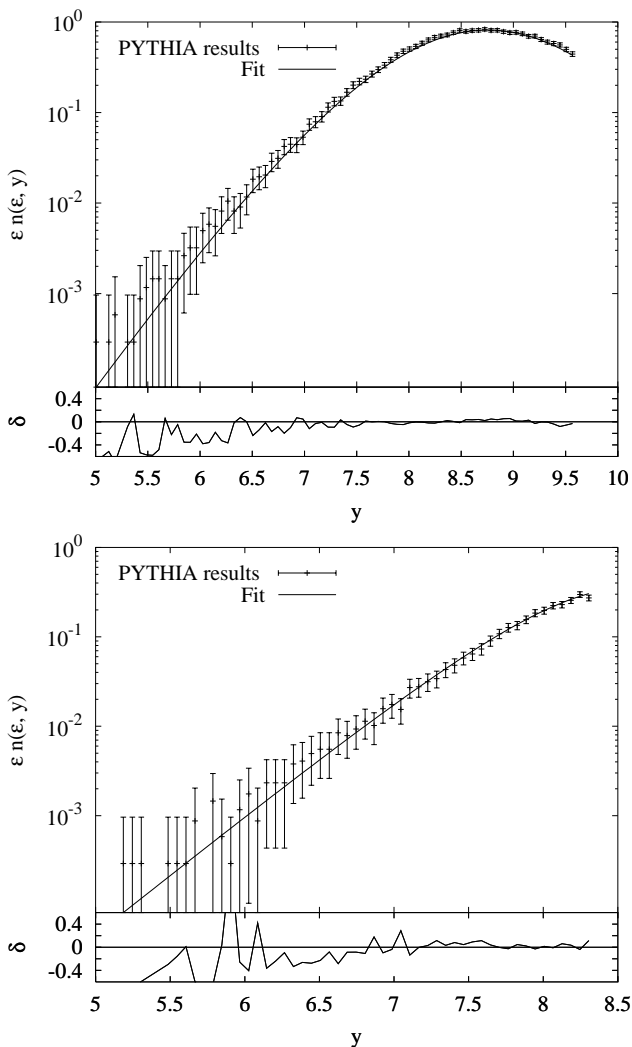


FIG. 4: Rapidity distributions of  $\pi^+$  (top panel) and  $K^+$  (bottom panel) secondaries created in a collision of a proton with energy  $E_p = 10^6$  GeV with a proton at rest. The secondary particle energy is taken to be  $\epsilon = 10^3$  GeV. Upper graphs: comparison of PYTHIA results and fit to the rapidity distribution  $\epsilon n(\epsilon, y)$  as a function of  $y$ ; lower graphs: deviation  $\delta_i = n(\epsilon_i, y_i)/n_i - 1$  between PYTHIA results and fitted values.

avoid cluttering of notation):

$$q_0 = q_{00} + q_{01}\xi^2; \quad (21a)$$

$$q_1 = q_{10} + q_{11}(\xi + q_{12})^2 + q_{13}\xi^4; \quad (21b)$$

$$q_2 = \ln(\epsilon) + q_{20} + q_{21}(\log(\epsilon) + 1) - 10^{q_{22} \log(E_p) \log(\epsilon/E_p)} + 10^{q_{23} \log(E_p) \log(m/\epsilon)}; \quad (21c)$$

$$q_3 = q_{30} + 10^{q_{31} + q_{32} \log(\epsilon)}, \quad (21d)$$

where we introduced the variable

$$\xi \equiv 2 \log(\epsilon) / \log(E_p) - 1. \quad (22)$$

Hence, we have parameterized the pion energy and rapidity distributions in terms of 24 free parameters  $q_{ij}$  for

every pion species ( $\pi^+$ ,  $\pi^-$  and  $\pi^0$ ). The fitted values for the coefficients are given in table IV.

Deviations between the parameterizations and PYTHIA results are within 10% in the range in which the rapidity distribution is within one order of magnitude of the maximum value and for pion energies  $1 \text{ GeV} < \epsilon < 0.1 E_p$ , except for a few isolated points that are typically within 20%. At high energies,  $\epsilon \geq 0.1 E_p$ , deviations increase to  $\sim 30\%$  at the borders of the considered rapidity interval, in concordance with eq. (14).

We have verified that integrating the energy and rapidity distributions over rapidity reproduces the energy spectra. The deviations between these spectra and PYTHIA results are similar to the deviations for the direct fit to the energy spectra (see section V C), except at very low energies  $\epsilon \lesssim 2m_\pi$  where deviations increase to  $\sim 30\%$ . The multiplicities obtained by integrating the distributions over energy and rapidity are within a few percent of those given by eq. (15).

## 2. Kaons

The shape of the kaon rapidity distributions is similar to the low-rapidity part of the pion rapidity distributions (see fig. 4). We find that the kaon energy and rapidity distributions are well described with:

$$n_K(\epsilon, y) = \bar{n}(\epsilon)\phi(\epsilon, y), \quad (23)$$

where  $\phi(\epsilon, y)$  is defined in terms of model parameters  $q_i$  in eqs. (20) and  $\bar{n}(\epsilon)$  is a modified energy spectrum:

$$\bar{n}(\epsilon) = n_0 \epsilon^{-1} \alpha(\epsilon) \beta(\epsilon) 10^{q_0 + 2q_3}. \quad (24)$$

The quantities  $n_0$ ,  $\alpha(\epsilon)$  and  $\beta(\epsilon)$  are defined in eqs. (17). We find that the parameterizations for  $q_i$  given in eqs. (21) approximate the PYTHIA results well if we fix  $q_{23} = 0$ . Therefore, the kaon energy and rapidity distributions are fully parameterized in terms of 23 free parameters for every kaon species ( $K^+$ ,  $K^-$ ,  $K^0$  and  $\bar{K}^0$ ). The fitted values for these parameters are presented in table IV.

Deviations between the approximation (23) and PYTHIA results are similar to the deviations for the parameterizations of the pion distributions, except that fluctuations are larger. This results in deviations up to  $\sim 30\%$  at isolated points for all energies.

For the  $K^-$  and  $\bar{K}^0$  mesons, integrating the full distributions over the rapidity reproduces the energy spectra with deviations similar to those for the direct parameterizations of the energy spectra presented in eq. (16). For  $K^+$  and  $K^0$  mesons, deviations near the mass threshold are  $\sim 30\%$ , while at very high energies ( $\epsilon \gtrsim E_p/2$ ) the deviations can increase to  $\sim 50\%$ . These large deviations occur only at energies where  $\epsilon n(\epsilon, y)$  is more than an order of magnitude smaller than the maximum value. The multiplicities obtained by integrating the parameterized distributions (23) over energy and rapidity are within a few percent of the values given by eq. (15).



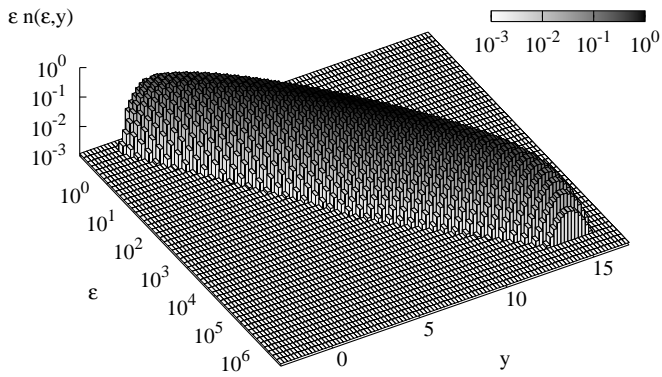


FIG. 5: The  $\pi^0$  distribution  $\epsilon n(\epsilon, y)$  as a function of energy  $\epsilon$  and rapidity  $y$  after a collision of a proton with energy  $10^6$  GeV with a proton at rest (lab frame). The discretization and the observed ‘floor’ are for presentational purposes.

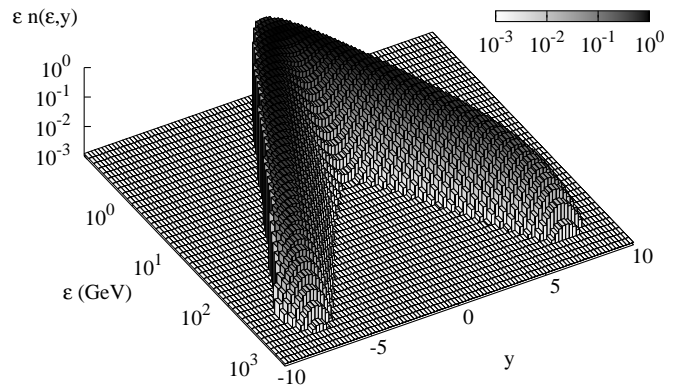


FIG. 6: The  $\pi^0$  distribution  $\epsilon n(\epsilon, y)$  as a function of energy  $\epsilon$  and rapidity  $y$  after a collision of two protons with energy 730 GeV (center-of-mass frame). The discretization and the observed ‘floor’ are for for presentational purposes.

## VI. APPLICATIONS

In this section, we consider applications of the parameterized particle distributions presented in eqs. (19) and (23). We show explicitly how the parameterizations can be used to study correlations between the energy and outgoing angle of secondary particles for a general scattering geometry, viz. two protons with different energies colliding at an arbitrary angle. We also present an example in which the energy spectrum of photons due to decay of  $\pi^0$  mesons created in a  $pp$  interaction is derived from the parameterized  $\pi^0$  distribution. For clarity, we consider only  $\pi^0$  mesons in this section, but the presented methods are applicable to all pions and kaons.

### A. Head-on proton – proton collision

#### 1. Full secondary particle distribution

First, we consider the energy and rapidity distribution of  $\pi^0$  mesons created in a collision of an energetic proton  $p$  with a fixed-target proton  $q$ . This is the scattering geometry for which the parameterizations presented in this work are derived. We denote the Lorentz frame corresponding to this scattering geometry with  $K$  throughout this section. In figure 5, we present the  $\pi^0$  distribution for incident proton energy  $E_p = 10^6$  GeV. We observe that the energy and rapidity of the secondary pions are strongly correlated: pions with higher energies are emitted closer to the direction of the incoming energetic proton (corresponding to higher values of the rapidity  $y$ ; see eq. (6)).

Next, we consider two protons  $p$  and  $q$  colliding head-on with energies  $E'_p$  and  $E'_q$  which defines the reference frame  $K'$ . Without loss of generality, we take the protons to be moving in the  $z'$  direction. The secondary particle

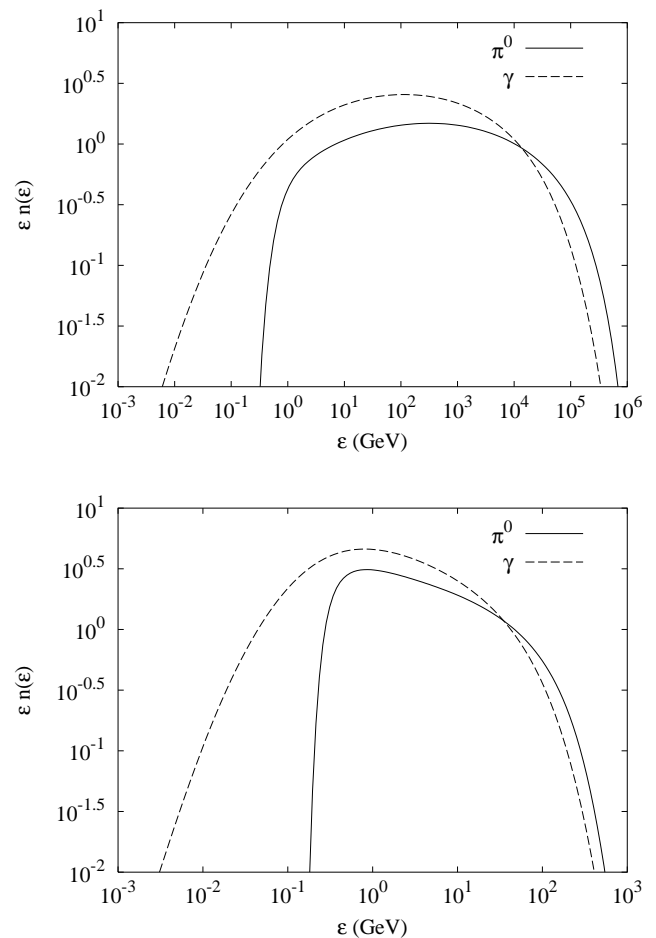


FIG. 7: Energy spectra of  $\pi^0$  mesons created in a  $pp$  collision and of the resulting gamma rays. Top panel: lab frame, corresponding to a proton with energy  $E_p = 10^6$  GeV colliding with a proton at rest; bottom panel: center-of-mass frame, corresponding to two protons with energy 730 GeV colliding head-on.

distribution in this frame is given by

$$n'(\epsilon', y') = \left( \frac{\epsilon' \cosh^2 y}{\epsilon \cosh^2 y'} \right) n(\epsilon, y), \quad (25)$$

which follows from eq. (12) and the invariance of  $\epsilon n(p_x, p_y, p_z)$ . In this equation,  $n(\epsilon, y)$  is the particle distribution in the frame  $K$  which is parameterized in eq. (19). Note that eq. (25) is only valid if the frames  $K$  and  $K'$  are connected with a single Lorentz boost in the  $z$  ( $z'$ ) direction, i.e. for protons colliding head-on along the  $z'$  axis in the  $K'$  frame.

As a concrete example, we consider two protons with equal energies  $E'_p = E'_q = 730$  GeV. In this case,  $K'$  coincides with the center-of-mass (COM) frame for a collision between a proton with energy  $E_p = 10^6$  GeV and a proton at rest. In particular, this means that the center-of-mass energy  $\sqrt{s}$  and the secondary multiplicities are identical for the scattering geometries in the frames  $K$  and  $K'$ .

In figure 6, we show the  $\pi^0$  energy and rapidity distribution after the collision in the COM frame  $K'$ . In this frame, the scattering geometry is invariant under the interchange of the two protons so that the secondary particle distribution is symmetric under the transformation  $y \rightarrow -y$ . It is observed from the figure that this is indeed the case for the distribution derived from the parameterization presented in this work. This is an *a posteriori* verification of the parameterization, which is derived in the lab frame without considering this symmetry.

## 2. Energy spectrum of secondary particles and decay products

In figure 7, we show the secondary  $\pi^0$  energy spectra for the scattering geometries associated with the  $K$  and  $K'$  frames, together with the gamma-ray energy spectra resulting from the decay  $\pi^0 \rightarrow \gamma\gamma$ . The decay spectrum  $n_\gamma(\epsilon_\gamma)$  is related to the pion spectrum  $n(\epsilon)$  as follows (see, e.g., Ref. [26]):

$$n_\gamma(\epsilon_\gamma) = 2 \int_{\epsilon_\gamma + m_\pi^2 c^4 / 4\epsilon_\gamma}^{\infty} \frac{n(\epsilon)}{\sqrt{\epsilon^2 - m_\pi^2 c^4}} d\epsilon, \quad (26)$$

where  $n(\epsilon)$  is the  $\pi^0$  energy spectrum. Because this formula is valid in all frames,  $n$  and  $\epsilon$  may be replaced by  $n'$  and  $\epsilon'$  to derive the gamma-ray energy spectrum from the pion energy spectrum in the  $K'$  frame.

## B. Proton – proton collision at an arbitrary angle

In this section, we consider two protons with energies  $E'_p$  and  $E'_q$  that collide at an arbitrary angle. Without loss of generality, we take proton  $p$  to be moving along the  $x'$  axis in the  $+x'$  direction and proton  $q$  to be moving in the  $x' - y'$  plane at an angle  $\phi'_p$  with respect to the  $x'$  axis.

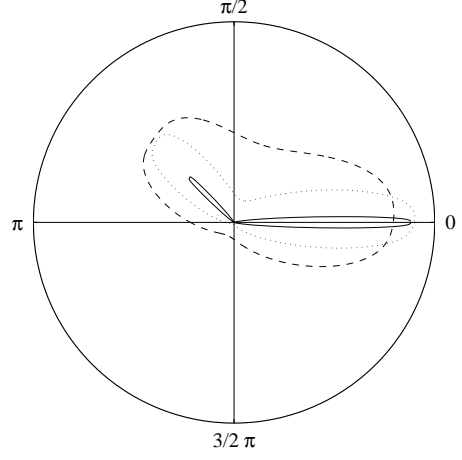


FIG. 8: Polar plot of the  $\pi^0$  distribution  $n'(\epsilon', \phi'_\pi)$  as a function of the azimuth angle  $\phi'_\pi$  after a collision of a  $10^4$  GeV proton with a  $10^2$  GeV proton at an angle  $\phi'_q = (3/4)\pi$ . We plotted the distribution for pion energies  $\epsilon' = 5$  GeV (solid line),  $\epsilon' = 1$  GeV (dotted line) and  $\epsilon' = 0.5$  GeV (dashed line).

We parameterize the distribution of secondary  $\pi^0$  mesons created in this interaction with the pion energy  $\epsilon'$ , the zenith angle  $\theta'_\pi$  (with respect to the  $z'$  axis) and the azimuthal angle  $\phi'_\pi$  (in the  $x' - y'$  plane). The pion momentum is thus expressed as follows:

$$k'_x = |\vec{k}'| \sin \theta'_\pi \cos \phi'_\pi; \quad (27a)$$

$$k'_y = |\vec{k}'| \sin \theta'_\pi \sin \phi'_\pi; \quad (27b)$$

$$k'_z = |\vec{k}'| \cos \theta'_\pi, \quad (27c)$$

where  $c|\vec{k}'| = \sqrt{\epsilon'^2 - m_\pi^2 c^4}$ . In the following, we derive the secondary  $\pi^0$  angular distribution in the scattering plane and the  $\pi^0$  energy spectrum.

### 1. Secondary angular distribution in the scattering plane

The pion distribution in the frame  $K'$  is derived from the parameterization in the fixed-target frame  $K$  by Lorentz transformations. The frames  $K'$  and  $K$  are connected by a Lorentz boost to the rest-frame of proton  $p$ , followed by a rotation to align the incoming proton  $q$  with the  $z$  axis. The number of secondary pions with energy and angles in the range  $(\epsilon' \dots \epsilon' + d\epsilon') \times (\theta'_\pi \dots \theta'_\pi + d\theta'_\pi) \times (\phi'_\pi \dots \phi'_\pi + d\phi'_\pi)$  is equal to  $n'(\epsilon', \theta'_\pi, \phi'_\pi) \sin \theta'_\pi d\theta'_\pi d\phi'_\pi d\epsilon'$ , where

$$n'(\epsilon', \theta'_\pi, \phi'_\pi) = \left( \frac{\epsilon \sqrt{\epsilon'^2 - m_\pi^2 c^4}}{m_\pi^2 c^4 + \epsilon^2 (1 - \tanh^2 y)} \right) \frac{n(\epsilon, y)}{2\pi}. \quad (28)$$

In this formula,  $\epsilon$  and  $y$  are the pion energy and rapidity in the  $K$  frame, respectively, and  $n(\epsilon, y)$  denotes the pion

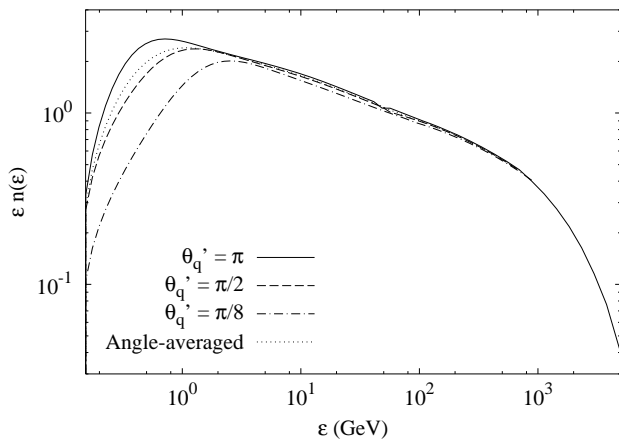


FIG. 9: Energy spectra of secondary  $\pi^0$  mesons created in a collision of a  $10^4$  GeV proton with a  $10^2$  GeV proton for three different incident angles  $\theta'_q$ . Also shown is the angle-averaged spectrum (see text). For numerical reasons we only plot the energy spectrum for head-on collisions at energies  $\epsilon \gtrsim 10^3$  GeV. We have verified with `PYTHIA` simulations that this part of the spectrum is independent of the incident angle between the protons.

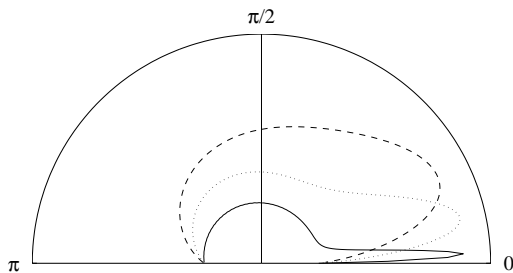


FIG. 10: Polar plot of the  $\pi^0$  distribution  $n'(\epsilon', \theta'_\pi)$  as a function of the zenith angle  $\theta'_\pi$  after a collision of a  $10^4$  GeV proton with an isotropic distribution of  $10^2$  GeV protons. The meaning of the lines is the same as in figure 8.

energy and rapidity distribution which is parameterized in eq. (19).

In figure 8, we present the distribution of secondary  $\pi^0$  mesons with respect to the azimuthal angle  $\phi'_\pi$ , i.e.,

$$n'(\epsilon', \phi'_\pi) \equiv \int_0^\pi n'(\epsilon', \theta'_\pi, \phi'_\pi) \sin \theta'_\pi d\theta'_\pi, \quad (29)$$

for different values of the pion energy  $\epsilon'$ . In producing this figure, we have chosen incident proton energies  $E'_p = 10^4$  GeV and  $E'_q = 10^2$  GeV and incident angle  $\phi'_q = (3/4)\pi$ . As can be seen from the figure, the pions are produced mostly in the direction of the incident protons. The degree of collimation is correlated with the energy: for pion energies  $\epsilon'$  below a few GeV, where the pion spectrum is highest (see fig. 9), the pion direction can be significantly different from the direction of the colliding

protons. At energies above a few GeV, the angle of the outgoing pion is typically within a few degrees of the direction of one of the colliding protons. We have verified that this result holds for all secondary pions and kaons.

## 2. Secondary energy spectrum

In figure 9 we present pion energy spectra (integrated over pion angles) resulting from a collision of two protons with energies  $E'_p = 10^4$  GeV and  $E'_q = 10^2$  GeV for different values of the proton collision angle  $\phi'_q$ . For comparison, we also show in this figure the pion spectrum averaged over incident proton angles (see below).

While the energy spectrum at high energies is independent of the incident proton angle, there are significant differences at low energies. For small values of the incident proton angle  $\phi'_q$ , i.e. close to a tail-on collision, the low-energy part of the spectrum is suppressed as expected.

## C. Isotropic distribution of target protons

In this section, we consider a single high-energy proton  $p$  with energy  $E'_p$  that interacts with an isotropic distribution (in three dimensions) of mono-energetic low-energy protons  $q$  with energy  $E'_q$ . We derive the distribution of secondary pions with respect to the angle between the high-energy proton and the pion, as well as the energy spectrum. For an isotropic distribution of target protons, the resulting pion distribution does not depend on the azimuthal angle around the direction of the high-energy proton. In order to keep the former definition of pion angles (eqs. (27)) we consider in this section a high-energy incident proton that moves along the  $z'$  axis in the  $+z'$  direction. With this choice, the zenith angle between the high-energy proton and the pion is equal to  $\theta'_\pi$ .

The momentum of proton  $q$  is expressed in terms of angles in the same way as the pion momentum in eqs. (27): the angle  $\theta'_q$  denotes the zenith angle with respect to the  $z'$ -axis and  $\phi'_q$  denotes the azimuthal angle with respect to the  $x'$  axis in the  $x' - y'$  plane.

### 1. Zenith angle distribution of secondary pions

The secondary pion distribution, averaged over the incoming angles of low-energy protons  $q$ , is given by the following expression:

$$\begin{aligned} \bar{n}'(\epsilon', \theta'_\pi, \phi'_\pi) &\equiv \frac{d^3 \bar{N}}{d\epsilon' d \cos \theta'_\pi d\phi'_\pi} \\ &= \frac{1}{\bar{\sigma}'_{\text{inel}}} \frac{d^3 \bar{\sigma}'}{d\epsilon' d \cos \theta'_\pi d\phi'_\pi}, \end{aligned} \quad (30)$$

where  $N$  is the total number of created pions,  $\sigma'_{\text{inel}}$  is the inelastic  $pp$  cross section and  $\sigma$  is the inclusive cross

section to detect a particle of a given species assuming an ideal detector (cf. section III B). In this section, we use a bar to indicate that a quantity is averaged over the incoming angles of low-energy protons  $q$ .

For clarity we assume in this section that both protons are very energetic, so that we may take  $\beta'_p = \beta'_q = 1$ . The averaged inelastic cross section is then equal to

$$\bar{\sigma}'_{\text{inel}} = \frac{1}{2} \int_0^\pi d\theta'_q \sin \theta'_q (1 - \cos \theta'_q) \sigma_{\text{inel}}(s(\theta'_q)). \quad (31)$$

In this equation,  $\sigma_{\text{inel}}$  depends on the proton angle  $\theta'_q$  through the center-of-mass energy  $\sqrt{s}$ , where

$$s(\theta'_q) = 2m_p c^2 + 2E'_p E'_q (1 - \cos \theta'_q). \quad (32)$$

The dependence of the inelastic cross section on  $s$  is expressed in eqs. (2) and (4).

For given values of the proton angles  $\theta'_q$  and  $\phi'_q$ , the differential inclusive cross section and the secondary particle distribution are related as follows:

$$\left. \frac{d^3 \sigma'}{d\epsilon' d \cos \theta'_\pi d\phi'_\pi} \right|_{\theta'_q, \phi'_q} = (1 - \cos \theta'_q) \sigma'_{\text{inel}}(s(\theta'_q)) \times n'(\epsilon', \theta'_\pi, \phi'_\pi; \theta'_q, \phi'_q), \quad (33)$$

where we have explicitly written the dependence of the pion distribution  $n'$  on the proton angles  $\theta'_q$  and  $\phi'_q$ . The total inclusive cross section  $\bar{\sigma}'$  is obtained by integrating eq. (33) over the outgoing pion angles and averaging over the incident proton angles. The resulting pion distribution is homogeneous in the  $\phi'_\pi$  variable. We use this rotational invariance to replace the integral over  $\phi'_q$  with a factor  $2\pi$  and choose the value  $\phi'_q = 0$  to find:

$$\bar{\sigma}' = \frac{1}{2} \int d\epsilon' d\theta'_\pi d\phi'_\pi \sin \theta'_\pi \int d\theta'_q \sin \theta'_q (1 - \cos \theta'_q) \times \sigma'_{\text{inel}}(s(\theta'_q)) n'(\epsilon', \theta'_\pi, \phi'_\pi; \theta'_q, \phi'_q = 0), \quad (34)$$

where the integrals cover the full phase space. The pion distribution with respect to the pion energy  $\epsilon'$  and scattering angle  $\theta'_\pi$  is defined as:

$$\bar{n}'(\epsilon', \theta'_\pi) = \frac{d^2 \bar{N}}{d\epsilon' d\theta'_\pi} = \sin \theta'_\pi \int_0^{2\pi} d\phi'_\pi \frac{d^3 \bar{N}}{d\epsilon' d \cos \theta'_\pi d\phi'_\pi} \quad (35)$$

Using eqs. (30) and (34), we find that

$$\bar{n}'(\epsilon', \theta'_\pi) = \frac{\sin \theta'_\pi}{2 \bar{\sigma}'_{\text{inel}}} \int_0^\pi d\theta'_q \sin \theta'_q (1 - \cos \theta'_q) \sigma'_{\text{inel}}(s(\theta'_q)) \times \int_0^{2\pi} d\phi'_\pi n'(\epsilon', \theta'_\pi, \phi'_\pi; \theta'_q, \phi'_q = 0), \quad (36)$$

where  $\bar{\sigma}'_{\text{inel}}$  is defined in eq. (31).

In figure 10 we show the distribution  $\bar{n}'(\epsilon', \theta'_\pi)$  as a function of  $\theta'_\pi$  for three different values of the pion energy  $\epsilon'$ . In producing this figure, we have considered a collision of an energetic proton with energy  $E'_p = 10^4$  GeV with an isotropic distribution of mono-energetic protons with

energy  $E'_q = 10^2$  GeV. From the figure we observe that pions with higher energy are collimated stronger within the direction of the incoming proton, as expected. We have verified that this holds for all secondary mesons. In the maximally forward direction, i.e., near  $\theta'_\pi = 0$ , the distribution decreases because the available phase space is proportional to  $\sin \theta'_\pi$ .

## 2. Energy spectrum of secondary pions

The secondary  $\pi^0$  energy spectrum for the interaction of a  $10^4$  GeV proton with the distribution of  $10^2$  GeV protons is expressed as

$$\bar{n}'(\epsilon') = \int_0^\pi d\theta'_\pi \bar{n}'(\epsilon', \theta'_\pi), \quad (37)$$

where  $\bar{n}'(\epsilon', \theta'_\pi)$  is given in eq. (36). We show in figure 9 the energy spectrum averaged over the incoming angles of the low-energy protons  $q$ . We find that the averaged spectrum is very close to the spectrum resulting from a collision of a  $10^4$  GeV proton with a  $10^2$  GeV proton with incident angle  $\theta'_q \simeq (5/8)\pi$ , i.e. in the forward direction but not head-on. Qualitatively, this is as expected because the cross section  $\sigma'_{\text{inel}}(s(\theta'_q))$  and the flux factor  $(1 - \cos \theta'_q)$  are largest for head-on collisions while the phase-space volume factor  $\sin \theta'_q$  suppresses head-on collisions.

## VII. EXTRAPOLATION TO THE HIGHEST COSMIC-RAY ENERGIES

The parameterizations presented in section V are based on simulated  $pp$  collisions for incident proton energies  $10^3$  GeV  $< E_p < 10^6$  GeV, where experimental data is available to verify the resulting particle distributions and multiplicities. Cosmic-ray observations suggest that the maximum proton energy that can be generated in astrophysical proton accelerators may be as high as  $10^{11}$  GeV. Thus, in order to account for interactions of the highest energy protons, the parameterizations presented in this work need to be applied in a region where they cannot be directly tested. In this section, we compare the high-energy behavior of the parameterizations derived in this work with an extrapolation of existing data and with theoretical models. Extrapolations of experimental data as well as theoretical models for incident proton energies  $E_p > 10^6$  GeV are available predominantly for the charged multiplicity, due to the availability of experimental data at lower energies. Therefore, we focus in this section on the charged multiplicity contained in the parameterizations presented in this work.

The charged multiplicity is dominated by pions, hence we estimate the charged multiplicity from the parameterized charged pion distributions. We derive the charged pion multiplicity  $\mathcal{M}_{\pi^\pm}^{\text{par}} = \mathcal{M}_{\pi^+}^{\text{par}} + \mathcal{M}_{\pi^-}^{\text{par}}$  by integrating eq. (19) over energy and rapidity. To account for

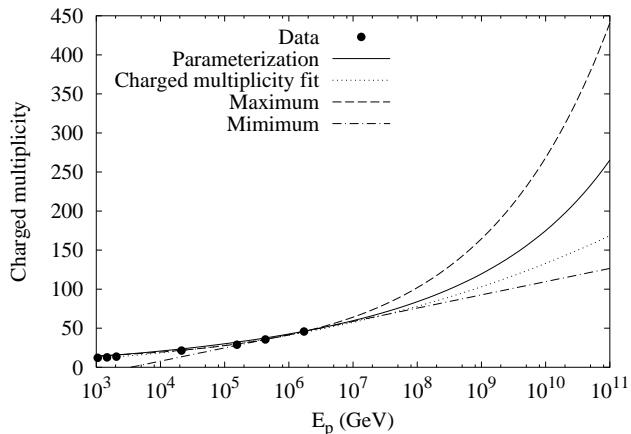


FIG. 11: Charged multiplicity as a function of incident proton energy. The solid line shows an extrapolation of eq. (5); the dotted line shows the multiplicity estimated from the parameterized charged pion distributions presented in this work; the dashed and dash-dotted lines show the minimum and maximum multiplicities given in eqs. (38). The data is taken from Refs. [37, 38, 39, 40, 41].

charged particle creation due to decay processes and for the contribution of other charged particles, we estimate the charged multiplicity with  $\mathcal{M}_{\text{ch}}^{\text{par}} = 2 + 1.47 \mathcal{M}_{\pi^\pm}^{\text{par}}$ , where the numerical value 1.47 is found by comparing  $\mathcal{M}_{\pi^\pm}^{\text{par}}$  and  $\mathcal{M}_{\text{ch}}$  at the proton energies considered in our simulations. The leading term 2 accounts for the number of outgoing protons for low secondary multiplicities (corresponding to low center-of-mass energies).

Using experimental data at low energies, Engel [49] has found that the charged multiplicity should increase faster than  $\log(s)$  but not as fast as  $s^p$ , where  $0.1 < p < 0.3$ , at high energies. In order to compare our results with these limiting cases, we have re-derived<sup>9</sup> the explicit functional form based on the two data points with highest energy [37, 40]:

$$\mathcal{M}_{\text{ch}}^{\text{min}} = -65 + 17 \log s; \quad (38a)$$

$$\mathcal{M}_{\text{ch}}^{\text{max}} = 7.0 + 1.4 s^{0.22}, \quad (38b)$$

where  $s$  is expressed in units of  $\text{GeV}^2$ . In figure 11 we show the charged multiplicity estimated from the parameterizations presented in this work, together with the minimum and maximum values of the multiplicity given in eqs. (38). Also shown is an extrapolation of the approximation  $\mathcal{M}_{\text{ch}}^{\text{fit}}$  given in eq. (5). We observe that the charged multiplicity estimated from our parameterizations increases faster than the extrapolation of  $\mathcal{M}_{\text{ch}}^{\text{fit}}$  but is well within the limits derived by Engel [49]. We thus

<sup>9</sup> The explicit form of these functions was not given in the original work [49]. The numerical value of 0.22 is chosen for comparison with fig. 8 of Ref. [49].

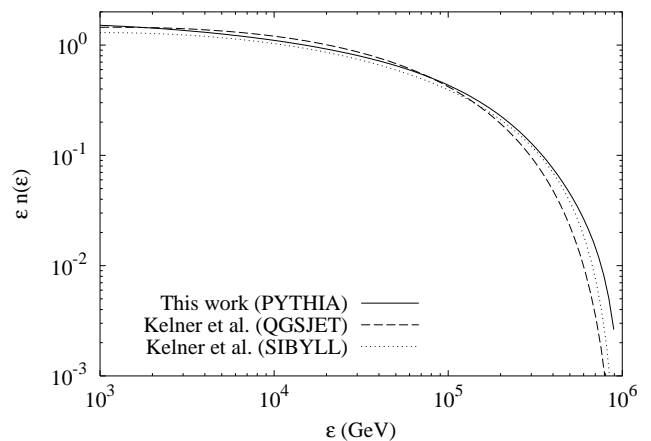


FIG. 12: Comparison of parameterizations of the  $\pi^0$  energy spectrum  $\epsilon n(\epsilon)$  for incident proton energy  $E_p = 10^6$  GeV. The energy range is chosen for comparison with fig. 1 of Ref. [24].

conclude that the high-energy behavior of the parameterizations presented in this work is consistent with theoretical expectations.

Applying the parameterizations presented in this work to very high proton energies  $E_p > 10^6$  GeV should be done with caution because there is no experimental data to directly test the results. Nevertheless, we estimate from figure 11 that the uncertainty in the charged particle multiplicity at the highest energies  $E_p \simeq 10^{11}$  GeV is less than a factor 2. While lacking experimental data on the full particle distributions at high energies, we find a strong similarity in the particle distributions for different proton energies within the three orders of magnitude in energy range considered in this work. This suggests that the shape of the distributions does not change significantly at very high energies so that the parameterizations derived in this work can be applied with some confidence to  $pp$  collisions with proton energies  $E_p > 10^6$  GeV.

## VIII. DISCUSSION

### A. Comparison with previous work

We have verified that the parameterizations of the pion and charged kaon distributions presented in this work are similar to those by Badhwar, Stephens and Golden [25] and Stephens and Badhwar [26] at the lowest energies considered in this work,  $\sqrt{s} = 45$  GeV. The difference between our parameterization of the neutral pion distribution and that of Blattnig et al. [27] is larger. These authors provide an accurate fit to the particle distribution at large transverse momentum. However, the number of particles in this region is very small and we find that the parameterization does not reproduce the total multiplicity correctly for center-of-mass energy  $\sqrt{s} = 45$  GeV.

In figure 12, we present a comparison of the parameterization of the  $\pi^0$  energy spectrum presented in this work with two parameterizations by Kelner, Aharonian and Bugayov [24]. These parameterizations are based on Monte Carlo results generated with QGSJET and SYBILL instead of PYTHIA. We observe from the figure that our parameterization is closer to the QGSJET fit at intermediate energies and closer to the SYBILL fit at high energies. The differences between the energy spectra described by the three parameterizations are up to  $\sim 10\%$  for intermediate pion energies. This is larger than the fit inaccuracy (see section V), which suggests that a more precise description of the energy spectra and particle distributions requires a better theoretical understanding of the  $pp$  physics, in particular of the fragmentation process, rather than more accurate fits.

The incomplete understanding of the collision physics is reflected in the availability of different tuning models for PYTHIA. Several tuning models for PYTHIA version 6.2 can be found in the literature, such as CDF tune A (Field<sup>10</sup>; see also Ref. [50]) or the tuning proposed in Ref. [51]. In this work, we have used PYTHIA 6.3 with default values. A preliminary tuning for PYTHIA version 6.3 is presented in Ref. [52]. It is our intention to adopt such a tuning after it has been extensively tested against the available data. In this work, we have not studied the effect of changing PYTHIA parameters, but we expect the differences in the resulting particle distributions to be comparable to the those resulting from the use of different Monte Carlo event generators (see fig. 12).

## B. Astrophysical applications

In section VI we demonstrated through explicit examples how the parameterizations presented in this work can be used to study particle creation in collisions of protons with different energies and an arbitrary incident angle. We found that the energy of secondary  $\pi^0$  mesons and the degree of collimation around the direction of the colliding protons are strongly correlated (see figures 8 and 10). We have verified that this holds for all secondary mesons. We expect that this has interesting observational consequences for neutrinos and gamma rays created in  $pp$  collisions in astrophysical sources.

In the early prompt emission of GRBs, the optical depth for  $pp$  interactions can be larger than a few. The mechanism responsible for the dissipation of the fireball energy may accelerate a substantial fraction of the protons contained in the fireball to high energies. Subsequent  $pp$  collisions give rise to high-energy neutrinos and gamma rays. Because the high-energy secondary mesons are collimated within the direction of the energetic pro-

ton, the energy and angular distribution of these secondaries depends on the distribution of the high-energy protons. Therefore, the resulting neutrino and gamma-ray signals may contain information about the details of the acceleration mechanism. We note however that in this scenario both interacting protons are moving toward an observer with ultra-relativistic velocities so that all particle distributions are collimated by relativistic beaming. This implies that also low-energy secondaries will be collimated in the observer frame and it will be difficult to extract information from the resulting signals. Nevertheless, the angle-energy correlations found in this work may make it possible to extract information about the acceleration mechanism.

The effect of energy-dependent collimation is particularly important for observations of secondary particles produced in  $pp$  collisions where the target proton is non-relativistic in the observer frame. A very interesting scenario in this respect is that of ‘failed GRBs’ [18, 19] (see also Refs. [53, 54]). It is possible that the mechanisms associated with the early phases of a developing GRB may be present in a large fraction of supernovae, but only lead to an observed GRB under special circumstances. For example, it may be the case that the formation of a fireball is quite a common phenomenon but that a large fraction of fireballs has insufficient energy to traverse the pre-burst stellar environment. However, if shocks form at a sub-stellar radius, protons can be accelerated and collide with target protons (nuclei). The resulting neutrinos are likely the only signals that could indicate the existence of such a class of failed (dark) GRBs. In this scenario, the energy and flux of the neutrinos that reach the earth depend strongly on the collimation of the secondary neutrinos created in the  $pp$  collisions.

## IX. CONCLUSION

In this paper we have studied the creation of secondary pions and kaons in energetic  $pp$  collisions using the event generator PYTHIA. We considered an incident proton with energy  $10^3 \text{ GeV} < E_p < 10^6 \text{ GeV}$  colliding with a target proton at rest. This corresponds to center-of-mass energy  $43 \text{ GeV} < \sqrt{s} < 1.4 \times 10^3 \text{ GeV}$ . The key result is the parameterization of the energy spectra (eq. (16)) and the energy and rapidity distributions (eqs. (19) and (23)) of secondary pions and kaons. Applications of these parameterizations are presented in section VI. In section VII, we have argued that the results can be applied to  $pp$  interactions for protons with energies  $E_p > 10^6 \text{ GeV}$ . At the highest CR energies,  $E_p \simeq 10^{11} \text{ GeV}$ , we have estimated the uncertainty in the parameterizations to be within a factor 2.

We have parameterized the particle distributions of meta-stable pions and kaons, as opposed to stable decay products, because this captures the essential properties of the  $pp$  interaction without making any assumptions about the importance of pion and kaon energy loss prior

<sup>10</sup> The CDF tune A is available at the website [http://www.phys.ufl.edu/~rfield/cdf/tunes/py\\_tuneA.html](http://www.phys.ufl.edu/~rfield/cdf/tunes/py_tuneA.html).

to decay (for concrete implications of pion decay in an astrophysical context, see e.g. Refs. [29, 30]). Energy spectra and full particle distributions of neutrinos and gamma rays are derived from the parameterizations presented in this work in a straightforward manner.

The energy and rapidity distributions fully describe the kinematics of the secondary mesons, so that the derived parameterizations contain all correlations between energy and angle of the outgoing particles and can be applied to a general scattering geometry, viz. two protons with different energies that collide under an arbitrary angle. Hence the parameterizations are not limited to collisions where one proton is at rest, which opens a wealth of astrophysical applications.

We presented in section VI several applications of the derived parameterizations. We derived the gamma-ray spectrum resulting from  $\pi^0$  decay after a  $pp$  collision (see figure 7) and we studied correlations between the energy and outgoing angle of secondary  $\pi^0$  mesons produced in a collision of two protons with different energies and arbitrary incident angle (see figure 8). These results can be used for a detailed study of  $pp$  interactions in the early prompt emission of GRBs and in the interaction of a developing GRB with its surroundings (see section VIII B). A particularly interesting possibility is the existence of a class of developing GRBs for which the fireball has insufficient energy to traverse the pre-burst stellar environment. If shocks are formed at a sub-stellar radius,

these will accelerate protons that collide with target protons and create neutrinos. The fluence and energy of neutrinos that reach the earth depend sensitively on the correlations between the energy and outgoing angle of the secondary mesons that are created in these  $pp$  interactions. The parameterizations presented in this work can be used to study this scenario in detail. We aim to investigate this in the future.

The parameterizations presented in this work can be extended with proton – neutron and proton – photon interactions, all of which can be studied with PYTHIA. The same holds for the energy spectrum and angular distribution of primary nucleons (the primary nucleon is the outgoing nucleon with the highest energy). This allows a more precise study of multiple nucleon – nucleon interactions. These parameterizations are left for future work.

### Acknowledgments

We wish to thank James Miller-Jones and Peter Mészáros for useful discussions. H. K. wishes to thank Justus Koch and Paul van der Nat for valuable discussions on hadron physics. This research was supported by NWO grant 639.043.302 to R.W. and by the EU under RTN grant HPRN-CT-2002-00294.

- 
- [1] F. Aharonian et al. (HESS Collaboration), *Astron. Astrophys.* **449**, 223 (2006).
  - [2] Y. M. Butt, D. F. Torres, J. A. Combi, T. Dame, and G. E. Romero, *Astrophys. J.* **562**, L167 (2001).
  - [3] O. Reimer, M. Pohl, Y. M. Butt, D. F. Torres, and G. E. Romero, *Astron. Astrophys.* **390**, L43 (2002).
  - [4] Atkins et al., *Astrophys. J.* **533**, L119 (2000).
  - [5] Atkins et al., *Astrophys. J.* **583**, 824 (2003).
  - [6] A. Pe’er and E. Waxman, *Astrophys. J.* **633**, 1018 (2005); Erratum-ibid. **638**, 1187 (2006).
  - [7] P. Bhattacharjee and G. Sigl, *Phys. Rept.* **327**, 109 (2000).
  - [8] F. Halzen, R. A. Vazquez, T. Stanev, and H. P. Vankov, *Astropart. Phys.* **3**, 151 (1995).
  - [9] P. L. Biermann, T. K. Gaisser, and T. Stanev, *Phys. Rev. D* **51**, 3450 (1995).
  - [10] V. Berezhinsky, A. Z. Gazizov, and S. I. Grigorieva, astro-ph/0210095.
  - [11] C. A. Norman, D. B. Melrose, and A. Achterberg, *Astrophys. J.* **454**, 60 (1995).
  - [12] J. P. Rachen and P. L. Biermann, *Astron. Astrophys.* **272**, 161 (1993).
  - [13] A. Venkatesan, M. C. Miller, and A. V. Olinto, *Astrophys. J.* **484**, 323 (1997).
  - [14] M. Vietri, *Astrophys. J.* **453**, 883 (1995).
  - [15] E. Waxman, *Phys. Rev. Lett.* **75**, 386 (1995).
  - [16] E. Waxman and J. Bahcall, *Phys. Rev. Lett.* **78**, 2292 (1997).
  - [17] M. Böttcher and C. D. Dermer, *Astrophys. J.* **499**, L131 (1998).
  - [18] P. Mészáros and E. Waxman, *Phys. Rev. Lett.* **87**, 171102 (2001).
  - [19] S. Razzaque, P. Mészáros, and E. Waxman, *Phys. Rev. D* **68**, 083001 (2003).
  - [20] J. Granot and D. Guetta, *Phys. Rev. Lett.* **90**, 191102 (2003).
  - [21] S. Razzaque, P. Mészáros, and E. Waxman, *Phys. Rev. Lett.* **90**, 241103 (2003).
  - [22] S. Razzaque, P. Mészáros, and E. Waxman, *Phys. Rev. D* **69**, 023001 (2004).
  - [23] T. Kamae, N. Karlsson, T. Mizuno, T. Abe, and T. Koi, *Astrophys. J.* **647**, 692 (2006).
  - [24] S. R. Kelner, F. A. Aharonian, and V. V. Bugayov, *Phys. Rev. D* **74**, 034018 (2006).
  - [25] G. D. Badhwar, S. A. Stephens, and R. L. Golden, *Phys. Rev. D* **15**, 820 (1977).
  - [26] S. A. Stephens and G. D. Badhwar, *Astrophys. Space Science* **76**, 213 (1981).
  - [27] S. R. Blattnig, S. R. Swaminathan, A. T. Kruger, M. Ngom, and J. W. Norbury, *Phys. Rev. D* **62**, 094030 (2000).
  - [28] F. Halzen and A. D. Martin, *Quarks and leptons* (John Wiley & Sons, Inc., 1984).
  - [29] T. Kashti and E. Waxman, *Phys. Rev. Lett.* **95**, 181101 (2005).
  - [30] K. Asano and S. Nagataki, *Astrophys. J.* **640**, L9 (2006).
  - [31] T. Sjöstrand, L. Lonnblad, S. Mrenna, and P. Skands, hep-ph/0308153.

- [32] B. Andersson, G. Gustafson, G. Ingelman, and T. Sjöstrand, Phys. Rept. **97**, 31 (1983).
- [33] U. Amaldi and K. R. Schubert, Nucl. Phys. B **166**, 301 (1980).
- [34] A. Breakstone et al. (Ames-Bologna-CERN-Dortmund-Heidelberg-Warsaw Collaboration), Phys. Lett. B **132**, 458 (1983).
- [35] P. D. B. Collins and A. D. Martin, *Hadron interactions* (Adam Hilger Ltd., Bristol, 1984).
- [36] G. Matthiae, in *Proceedings of HEP83, Brighton, 1983*, edited by J. Guy and C. Costain.
- [37] R. E. Ansorge et al. (UA5 Collaboration), Z. Phys. C **43**, 357 (1989).
- [38] K. Alpgard et al. (UA5 Collaboration), Phys. Lett. B **121**, 209 (1983).
- [39] J. Benecke et al. (Bonn-Hamburg-Munich Collaboration), Nucl. Phys. B **76**, 29 (1974).
- [40] M. Biyajima, T. Mizoguchi, N. Nakajima, A. Ohsawa, and N. Suzuki, Phys. Lett. B **515**, 470 (2001).
- [41] A. Breakstone et al. (Ames-Bologna-CERN-Dortmund-Heidelberg-Warsaw Collaboration), Phys. Rev. D **30**, 528 (1984).
- [42] W. M. Morse et al., Phys. Rev. D **15**, 66 (1977).
- [43] C. S. Lindsey et al. (E735 Collaboration), Nucl. Phys. A **544**, 343c (1992).
- [44] M. Antinucci et al., Lett. Nuovo Cim. **6**, 121 (1973).
- [45] Z. Koba, H. B. Nielsen, and P. Olesen, Nucl. Phys. B **40**, 317 (1972).
- [46] G. J. Alner et al. (UA5 Collaboration), Phys. Lett. B **138**, 304 (1984).
- [47] G. J. Alner et al. (UA5 Collaboration), Phys. Lett. B **167**, 476 (1986).
- [48] R. P. Feynman, Phys. Rev. Lett. **23**, 1415 (1969).
- [49] R. Engel, Nucl. Phys. B (Proc. Suppl.) **75A**, 62 (1999)
- [50] C. M. Buttar et al., in Proceedings Part A HERA and the LHC: a workshop on the implications of HERA for LHC physics, 2005, edited by A. De Roeck and H. Jung, CERN-2005-014, hep-ph/0601012.
- [51] C. M. Buttar, D. Clements, I. Dawson and A. Moraes, Acta Phys. Pol. B **35**, 433 (2004).
- [52] A. Moraes and C. M. Buttar, in Proceedings of the Les Houches Workshop on Physics at TeV Collider, 2006, edited by G. Belanger, F. Boudjema, J.-P. Guillet, and E. Pilon, hep-ph/0604120.
- [53] S. Razzaque, P. Mészáros, and E. Waxman, Mod. Phys. Lett. A **20**, 2351 (2005).
- [54] S. Razzaque, P. Mészáros, and E. Waxman, Phys. Rev. Lett. **93**, 181101 (2004); Erratum-ibid. **94**, 109903 (2005).
- [55] Schwinger, J. S., Phys. Rev. **82**, 664 (1951).

## APPENDIX A: THE LUND STRING MODEL

The Lund string model [32] is an iterative model used in PYTHIA to describe meson formation after a hard QCD process. In the model, quark-antiquark pairs that are created in a hard QCD scattering process form ‘strings’ that are connected through a color flux-tube with energy per unit length  $\kappa$ . This string breaks into a meson and a remainder string that will undergo the same process (baryons are generated through a generalization of this process). At every step in the iteration, a meson is created with a certain energy and rapidity according to a probability distribution.

The mechanism to break the string is the creation of a new quark-antiquark pair through quantum-mechanical tunneling. The probability to create a  $q\bar{q}$  pair with mass  $m$  and transverse momentum  $p_T$  is given by

$$\mathcal{P} = \exp\left(-\frac{\pi}{\kappa}(m^2c^4 + p_T^2c^2)\right), \quad (\text{A1})$$

which derives from the Schwinger formula [55]. This implies that lighter mesons are created more prolifically than heavier mesons and that the probability to create a meson falls off exponentially with increasing  $p_T$ . After a meson is created, the probability that it carries a fraction  $z$  of the string’s  $E + p_z$  is determined by the so-called fragmentation function [31, 32]. Together with eq. (A1), this fragmentation function determines the secondary particle distributions. Free parameters within the model are adjusted to reproduce experimental data. A detailed description can be found in Refs. [31, 32].



TABLE III: Numerical values of the energy spectrum fit parameters  $p_{ij}$ .

	$\pi^+$	$\pi^-$	$\pi^0$	$K^+$	$K^-$	$K^0$	$\overline{K^0}$
$p_{00}$	-0.497	-0.501	-0.456	-1.23	-1.46	-1.29	-1.50
$p_{01}$	0.0934	0.0934	0.0950	0.0657	0.101	0.0690	0.101
$p_{10}$	-0.140	-0.128	-0.142	-0.147	-0.109	-0.142	-0.118
$p_{11}$	0.0131	0.0118	0.0135	0.0161	0.00865	0.0154	0.0101
$p_{20}$	-0.455	-0.437	-0.457	-0.00411	-0.0577	-0.00717	-0.0567
$p_{21}$	0.495	0.494	0.494	0.493	0.491	0.493	0.491
$p_{30}$	-2.06	-0.945	-1.49	-0.989	-1.22	-1.03	-1.25
$p_{40}$	-0.896	-1.03	-0.981	-0.345	-0.164	-0.294	-0.169
$p_{50}$	1.11	0.963	1.01	0.777	1.04	0.839	1.05
$p_{60}$	0.791	0.598	0.723	-0.235	-0.279	-0.272	-0.272
$p_{70}$	37.7	15.3	22.1	42.7	18.6	33.8	21.2
$p_{80}$	7.69	7.23	8.53	12.0	4.23	10.1	4.07

TABLE IV: Numerical values of the energy and rapidity distribution fit parameters  $p_{ij}$  (refitted modified energy spectrum) and  $q_{ij}$ . A hyphen indicates that the parameter is not used in the parameterization.

	$\pi^+$	$\pi^-$	$\pi^0$	$K^+$	$K^-$	$K^0$	$\overline{K^0}$
$p_{00}$	-0.474	-0.461	-0.420	-1.03	-1.20	-1.13	-1.37
$p_{01}$	0.0846	0.0796	0.0821	-0.00299	0.0377	0.0168	0.0501
$p_{10}$	-0.115	-0.124	-0.118	-0.0375	-0.0291	-0.0604	-0.0579
$p_{11}$	0.0102	0.0117	0.0107	0.00396	-0.000110	0.00621	0.00351
$p_{20}$	-0.560	-0.604	-0.598	-0.835	-0.606	-0.655	-0.467
$p_{21}$	0.497	0.496	0.497	0.494	0.497	0.497	0.497
$p_{30}$	-1.15	-0.641	-0.815	-0.742	-0.845	-0.788	-0.917
$p_{40}$	-1.03	-1.11	-1.17	-0.167	-0.155	-0.237	-0.176
$p_{50}$	1.12	0.980	0.987	0.716	0.934	0.840	1.01
$p_{60}$	0.962	0.891	0.954	1.08	0.597	0.789	0.371
$p_{70}$	-	-	-	-	-	-	-
$p_{80}$	6.98	6.93	7.45	-	-	-	-
$q_{00}$	-0.167	-0.149	-0.161	0.539	0.363	0.405	0.382
$q_{01}$	0.0497	0.108	0.0737	0.222	0.228	0.149	0.195
$q_{10}$	0.668	0.668	0.637	0.889	1.06	0.997	1.12
$q_{11}$	0.329	0.328	0.307	0.523	0.673	0.612	0.719
$q_{12}$	0.116	0.0806	0.107	0.227	0.328	0.216	0.298
$q_{13}$	-0.162	-0.154	-0.144	-0.304	-0.141	-0.306	-0.155
$q_{20}$	2.03	2.05	2.16	0.902	0.695	0.676	0.579
$q_{21}$	-0.0577	-0.0654	-0.0704	-0.0694	-0.0648	-0.0525	-0.0527
$q_{22}$	0.247	0.233	0.216	0.185	0.226	0.242	0.261
$q_{23}$	0.665	0.381	0.556	0	0	0	0
$q_{30}$	1.04	1.24	1.37	0.319	0.198	0.238	0.184
$q_{31}$	3.94	4.51	4.92	1.16	1.17	0.951	1.08
$q_{32}$	-1.37	-1.54	-1.65	-0.597	-0.699	-0.559	-0.684